Title

Reservoir scale reactive-transport modeling of a buoyancy-controlled CO_2 plume with impurities (SO_2, NO_2, O_2)

Authors

Spycher, Nicolas F
Llanos, Ella María
Vu, Hong P
et al.

Publication Date

2019-10-01

DOI

10.1016/j.ijggc.2019.06.026

Peer reviewed

International Journal of Greenhouse Gas Control 89 (2019) 40–51

Reservoir Scale Reactive-Transport Modeling of a Buoyancy-Controlled CO_2 Plume with Impurities (SO_2, NO_2, O_2)

Nicolas F. Spycher[1], Ella María Llanos[2], Hong P. Vu[2], Ralf R. Haese[2]

[1]Lawrence Berkeley National Laboratory, Berkeley, California, U.S.A

[2]Peter Cook Centre for CCS Research, The University of Melbourne, Melbourne, Australia
e-mail: nspycher@lbl.gov

ABSTRACT

A demonstration project for the geological storage of CO_2 is currently being considered in the deep Precipice Sandstone formation of the Surat Basin, Queensland, Australia. Because of the presence of potential fresh water resources in this formation, a reservoir-scale two-dimensional reactive-transport model was developed to assess temporal and spatial changes in water quality imposed by co-injecting CO_2 with SO_2, NO_2, and O_2 at this location. The model shows that because the injection rate is low (60 tons/year), flow is buoyancy-dominated and under these conditions the predicted CO_2 flow pattern is quite sensitive to fine-scale heterogeneities and the resolution of the numerical mesh. The model also shows that SO_2 and NO_2 readily partition into the aqueous phase in close vicinity of their injection point, lowering pH somewhat beyond the acidification from CO_2 dissolution. Only O_2 under redox disequilibrium conditions is modeled to persist in the CO_2 plume away from the injection point, however at sub-ppm levels. This modeling effort demonstrates acidification near the wellbore due to the preferential stripping of gas impurities, and accumulation of CO_2 around a lithostratigraphic boundary above the target formation, where relatively rapid mineral dissolution (muscovite, chlorite and calcite) and precipitation (ankerite, kaolinite and chalcedony) occur.

1. INTRODUCTION

1.1. Background and objectives

Site-specific assessments are being conducted by the Australian Carbon Transport and Storage Company (CTSCo) to better understand the physical and chemical changes introduced by the injection and storage of CO_2 into a deep sandstone formation of the Surat Basin, SE Queensland, Australia (Glenhaven Site, Figure 1). The prospective storage reservoir is the Lower Jurassic Precipice Sandstone, which is the deepest groundwater aquifer in the Surat Basin, with potable water quality. The lower Precipice Sandstone is approximately 70 m thick at the Glenhaven site. It consists primarily of high porosity and high permeability stacked channel deposits with large amounts of quartz (> 90 %) and is essentially devoid of carbonate minerals. In contrast, the upper Precipice Sandstone sediments are lower in porosity and permeability and contain less quartz and more feldspar, chlorite and calcite than the lower sandstone.

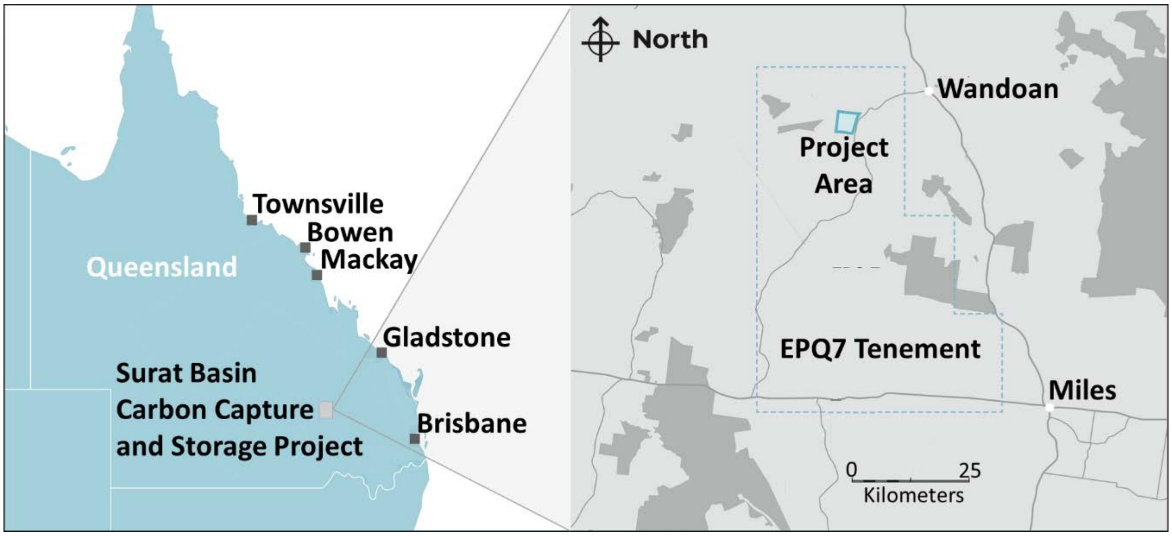

Figure 1. Map of SE Queensland showing major CO_2 emission points in form of coal fired power plants and the Glenhaven Site within the EPQ7 tenement. Figure kindly provided by CTSCo.

The present study was undertaken to assess the migration extent of free-phase and dissolved CO_2 with impurities around a planned injection well into the lower Precipice Sandstone. A series of simulations were performed considering fine-scale hydrologic and mineralogical heterogeneities, various near-wellbore spatial discretization (Table 1), and a range of residual gas saturation values and other parameters affecting the calculation of capillary pressure and relative permeability (Tables 1 to 5). The objective of this modeling effort was to evaluate: a) what properties in a multi-phase transport model determine whether buoyancy-dominated CO_2 migration occurs in channelized flow paths as opposed to one homogeneous plume, b) what controls migration and reactions of CO_2 impurities (SO_2, NO_2, O_2) and where do CO_2 impurities accumulate in the reservoir, and c) whether carbon mineralization should be expected and at what locations. The details of this study have been reported in a confidential report (Spycher et al., 2018), of which key aspects are summarized in this paper.

1.2. Relevant previous studies

The effects of impurities usually present in flue gas such as NO_2 and SO_2 have been the subject of significant interest because these produce acid rain, and their removal from emissions adds significantly to the cost of CO_2 capture. We discuss here previous modelling and experimental studies considering these and other impurities in the context of carbon geologic storage, focusing on those most relevant to the present study. Islam and Chakma (1993) were among the first authors to present such simulations. Their modeling study dealt with storage capacity in depleted oil and gas fields, focusing on the potential effect of impurities on the miscibility of CO_2 in oil. Perkins and Gunter (1995) and Gunter et al. (2000) modeled the reactions of CO_2 and, separately, of acid gases, upon their injection into the subsurface, however without considering transport. Nevertheless, their work provided a good first understanding of the potential for reactive minerals in carbonate and sandstone aquifers (e.g. calcite, plagioclase, chlorite) to neutralize acids (H_2CO_3, H_2S, H_2SO_4) resulting from the co-injection of CO_2 with H_2S and SO_2, accompanied by precipitation of secondary carbonate and clay minerals, as well as potentially sulfates at elevated SO_2 concentrations. Knauss et al. (2005) reported on reactive-transport simulations of CO_2 and impurities in a sandstone formation, by modelling the one-dimensional transport and reaction of an aqueous fluid equilibrated at its source with CO_2 as well as with H_2S and SO_2 as co-injectates. Their results showed minimal effects from H_2S co-injection even at elevated concentrations (11 vol. %), but a significant acidification beyond that from CO_2 alone resulting from small amounts of SO_2 oxidation (11 ppbv). Xu et al (2007) expanded on the complexity of these simulations by modeling the injection (two-dimensional radial) of supercritical CO_2 with either H_2S (1.3 wt. %) or SO_2 (~2.4 wt. %) into a deep saline aquifer. In their case, the impurities were also modeled as species dissolved into water co-injected with supercritical CO_2, with a focus on their effect on pH and porosity, which directly relates to injectivity. These authors reached similar conclusions as Knauss et al. (2005) and previous investigators, notably that co-injection of H_2S should not significantly impact injection, but that SO_2 oxidation could result in significant acidification and porosity decrease (by anhydrite precipitation) in the vicinity of the injection point. Their simulations also supported earlier geochemical modeling work by Palandri and Kharaka (2005), later confirmed experimentally by Garcia et al. (2012) and Pearce et al. (2015), showing that H_2S and SO_2 can drive the reductive dissolution of Fe(III) minerals and precipitation of Fe(II) carbonates and sulfides, thereby fixing both CO_2 and sulfur compounds.

Similar two-dimensional radial reactive-transport simulations of CO_2 injection with impurities have since been carried out by Wolf et al. (2016) (1 vol.% SO_2) and Todaka and Xu (2017) (67 ppmv SO_2, 9 ppmv NO_2, and 6150 ppmv O_2), also treating impurities as aqueous species in water co-injected with CO_2. Modeling co-injectants as gaseous compounds within the injected CO_2 phase, Spycher and Oldenburg (2014) assessed the effect of mercury co-injection (190 ppbv) with CO_2, with and without hydrogen sulfide (H_2S, 200 ppmv). Their study suggested a negligible impact of mecury and H_2S on water quality and injectivity, with precipitation of cinnabar (HgS) primarily at the edge of the free-phase CO_2 plume.

Talman (2015) presented a review of impurities expected in CO_2 streams and their phase partitioning behaviour in deep saline aquifers, as well as thermodynamic analyses of their effect on host aquifers. Waldmann and Rütters (2016) used geochemical modelling to further evaluate the impact of SO_2 (50 ppmv) on the performance of geological CO_2 storage in the Rotliegend Sandstones. Like previous investigators, they reported significant pH lowering from produced sulfuric acid, accompanied by the precipitation of secondary sulfate minerals. Modeling and experimental work by Thaysen et al. (2017) further examined the effect of calcite dissolution concomitant with gypsum precipitation for cases of higher SO_2 concentrations (0.4 vol.%) co-injected with CO_2 in limestone, sandstone and marl sediments. In the context of demonstrating their simulator capabilities, Sin et al. (2017) presented generic simulations of CO_2 co-injection with H_2S (25 vol.%) in a carbonate aquifer, illustrating the strong pH buffering and H_2S chromatographic separation reported in previous studies. Batch reactor experiments and geochemical modelling by Hedayati et al. (2018) investigated the reaction of N_2 and separately CO_2, both containing SO_2 (1.5 vol.%) with samples from the Heletz Sandstone Formation, Israel.

This study also showed significant acidification below that from pure CO_2 but without clear detection of secondary minerals predicted by modeling. Push-pull well tests and geochemical modeling were conducted by Vu et al. (2017, 2018) at the Otway site in Australia to investigate the geochemical impact of NO_2, SO_2 and O_2 on water-rock interactions in this siliciclastic reservoir. The effect of these impurities on water quality and mineral alteration was not significant, mainly because of the natural buffering capacity of the formation water. The decrease in pH from SO_2 and NO_2 disproportionation caused the dissolution of iron-bearing minerals such as siderite, coupled to oxidative dissolution of pyrite and precipitation hematite when O_2 was co-injected with the CO_2.

To our knowledge, all previous reservoir-scale reactive-transport modeling studies of CO_2 injection in the context of carbon geologic storage considered either fully- or laterally-homogenous aquifer hydrologic and mineralogical properties. The effect of fine-scale hydrologic heterogeneity on CO_2 flow has been previously investigated with multiphase flow simulations, however without chemical reactions (Saadatpoor, 2009; Saadatpoor et al., 2009). These authors showed capillary heterogeneity to be an important process leasing to channeling and increased residual trapping of CO_2 in the case of buoyancy-driven CO_2 plumes, similar to conditions applying to the present study.

2. NUMERICAL MODEL DEVELOPMENT

2.1. Reactive-transport simulator and main model simplifications

Flow and reactive-transport simulations were carried out with TOUGHREACT-OMP V3.32 (Sonnenthal et al., 2014; Xu et al., 2011) in tandem with the ECO2N V1.0 module (Pruess and Spycher, 2007) for water and CO_2 flows. The thermodynamic and kinetic data necessary for these simulations are described in Appendix A. The simulator was applied to model flow, transport, and reaction of supercritical CO_2 and impurities (SO_2, NO_2, and O_2) in initially fully water-saturated, porous, sedimentary rocks. The simulated coupled processes include multiphase flow and reactive-transport of multiple chemical components in both the aqueous and compressed "gaseous" phases, including kinetically controlled mineral precipitation/dissolution together with aqueous speciation and gas dissolution/exsolution at local equilibrium. The kinetically controlled dissolution of gaseous impurities was also considered in some cases. Porosity and permeability were dynamically coupled to mineral precipitation and dissolution using the Kozeny-Carman equation. Heat transport and heat effects from chemical reactions, including gas dissolution, were assumed negligible and thus not considered. Because of the low salinity of the groundwater (~ 200 mg/L TDS), the effect of dissolved salts on the flow and phase partitioning of CO_2 and H_2O was also deemed negligible.

The potential impact of impurities (SO_2, NO_2, and O_2) on the solubility and physical properties of injected CO_2 was not considered because only ppm-level concentrations of these trace gases were modeled. For SO_2 this assumption appears supported by Miri et al. (2014), who show that for concentrations below 5% in CO_2, the change of gas solubility in water is negligible, despite an exponential behaviour of the solubility CO_2 in water with respect to concentrations of SO_2. Tan and Piri (2013) point out that NO_2 reacts almost immediately with H_2O upon dissolution, preventing direct solubility measurements, suggesting that small concentrations of this compound in CO_2 are not expected to affect gas phase properties significantly. For simplicity these impurities were also assumed to follow an ideal behaviour (unit fugacity coefficients) in the CO_2-dominant phase. The effect of this assumption was assessed using a non-ideal phase partitioning model (Ziabakhsh-Ganji and Kooi, 2012) and deemed of second-order importance when considering the variability and uncertainty of many of the model inputs.

Simulations were performed on vertical 2-D cross-sections that account for sufficient geologic detail and heterogeneities at a relatively small scale, while keeping the size of the numerical mesh to a manageable size to minimize computational time. A correction was applied to the CO_2 injection flow rate to best mimic injection within a three-dimensional domain. The applied correction factor (the ratio of a rectangular area, $2r\Delta y$, to a circular area πr^2) in essence ensured that, for the same injected volume, the horizontal extent r of the CO_2 plume in 2-D cross-sections would not exceed that of a 3D (radial) plume.

The wetting characteristics of the CO_2 plume were computed without hysteresis, using capillary pressure and relative permeability curves as a function of saturation that were fitted from the drainage data of a hysteretic model. However, residual saturation values from imbibition data were also tested with the model.

2.2. Model domain and discretization

Two representative vertical cross-sections were selected from a 3-D geologic Petrel™ site model provided by CTSCo. The cross-section with the highest geologic dip was chosen, because supercritical CO_2 is known to migrate by buoyancy along stratigraphic contacts between formations of contrasting permeability. Because the geology and simulation results were similar along both modeled cross-sections, this paper focuses only on one of them.

The top boundary of the numerical model was set about 25 meters above the base of the upper Precipice Sandstone and assumed closed to flow and transport on the basis of the low permeability of overlying sediments (Figure 2). The bottom of the model domain was set at the contact between the lower Precipice Sandstone and the underlying low-permeability Moolayember Formation; it was also assumed closed to flow and transport (Figure 2). Horizontally the model domain extends for 3 kilometers (from x = 0 to 3000 m), although all results in this paper are shown on a smaller horizontal scale (mostly from x = 600 to 2200 m) for better detail near the injection well. The model right and left boundaries were determined to be significantly outside the influence of the injection well and consequently set to constant ambient conditions of temperature, pressure, and formation-water composition.

The Petrel™ geologic grids provided by CTSCo contained information following a regular ΔX spacing of 25 m, and ΔZ spacings varying with location between 0.02 and 5 m, resulting in a large number of grid points (> 40,000). To minimize computation time, the spatial discretization of the numerical mesh was determined on the basis of two criteria: 1) limit the size of the numerical mesh to a maximum of 15,000 gridblocks and 2) maximize accuracy by refining the mesh as much as possible close to the injection well, while progressively relaxing the need for detail and accuracy at distances further away from the well. A number of spatial discretizations were tested, and two were retained: a “Fine” case, and a “Coarse” case (Table1, Figure 2). In the Fine grid case, the Δx spacings vary and are significantly refined near the well compared to the Petrel™ geologic model. In contrast, the same regular Δx spacing as the Petrel™ model were used for the Coarse grid case. In both grids, the same variable Δz spacings were adopted, with a vertical resolution significantly coarser than the geologic grid at most locations (Table 1). The well perforated interval was represented by three grid blocks, each with a Δz of 1 m, and Δx either 0.25 m (Fine grid) or 25 m (Coarse grid) (Table 1).

Table 1 Numerical model grid spatial discretization (see Figure 2)

Distance from Well Axis (m)	**Fine Grid Case ΔX (m)**	**Coarse Grid Case ΔX (m)**
0	0.25	25
25	0.125 – 5	25
25 – 110	5	25
110 – 325	10	25
325 – 500	10 – 50	25
500 – 1300	50	25
1300 – 2500	50 – 500	25
Depth (m BMSL)	**Fine Grid Case ΔZ (m)**	**Coarse Grid Case ΔZ (m)**
Surface – 935	1	1
935 – 1005	2	2
1005 – 1011*	1	1
1011 – 1300	1 – 50	1 – 50
Petrel Model Cross-Section ID	**Total Gridblocks**	**Total Gridblocks**
J-69	10943	11270

*Perforated section from 1007 to 1010 m below mean sea level (BMSL)

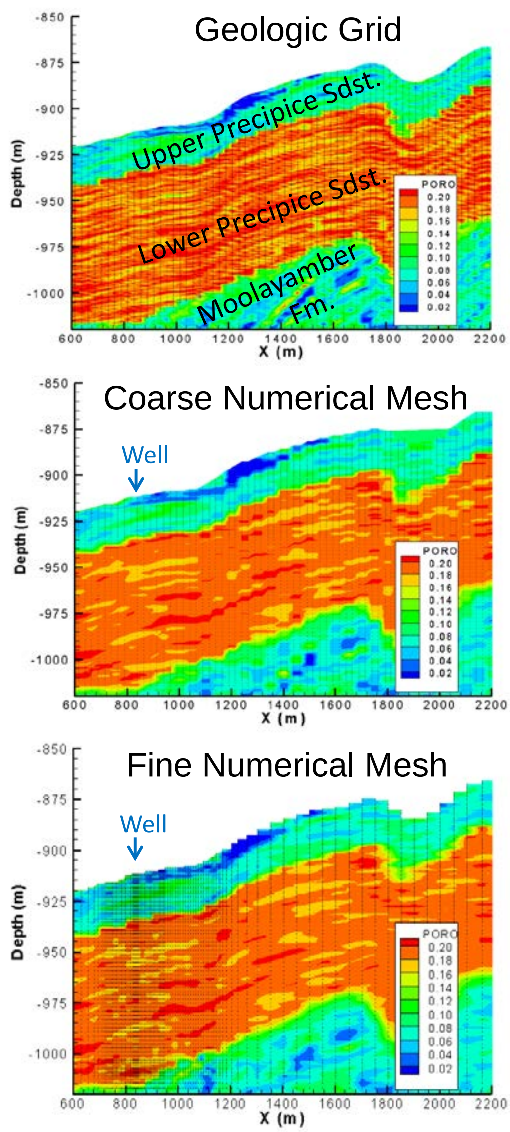

Figure 2. Close-up of the geologic grid and numerical meshes (Coarse and Fine cases), showing porosity, adopted for reactive-transport modelling of CO_2 injection at the well location shown (the injection interval is located at Z = -1010 to -1007 m, centered at X = 837.5 m). The full model domain extends from X = 0 to 3000 m, and Z = -852 to -1300 m BMSL.

2.3. Flow properties, mineralogy, and concentrations of impurities

Simulations were performed with fully heterogeneous (grid block by grid block) fields of permeability, porosity, and mineralogy developed from the provided Petrel™ geologic cross-sections of the site (Figure 2). The effect of varied capillary pressure resulting from these heterogeneous properties was captured by computing capillary pressure as a function of either local or site-wide average permeability and porosity values, applying the Leverett scaling relationship (Slider, 1976). Different combinations of these properties and spatial discretizations were tested, as summarized in Table 2 (Cases A, A1, B, B1).

Table 2. Simulated cases considered

Simulation Specifics	**Case A**	**Case A1**	**Case B**	**Case B1**
Numerical Mesh	Coarse	Fine	Fine	Fine
Gas residual saturation[(a)]	Low	Low	High	High
Average properties[(b)]	Local	Local	Local	Site-wide
Flow-only	X	X	X	X
RT, CO_2 only	X			X
RT, CO_2+NO_2+SO_2 [(c)]	X			
RT, CO_2+NO_2+SO_2+O_2	X		X	X
Dissolution of gas impurities	Equilibrium		Kinetics	Kinetics
Additional Sensitivity Runs:				
Higher impurities[(d)]	X			
0.1x and 10x surface areas	X			
Kinetic gas dissolution	X			

RT stands for Reactive-Transport

(a) Low: linear decrease from 0.2 to 0.08 from fine to coarse units; High: 0.27-0.47 (from imbibition data).

(b) Average permeability and porosity values used for Leverett Scaling; Local: averages taken over the modeled cross-section domain; Site-wide: average for the entire site.

(c) Target concentrations in CO_2 (ppmv): O_2, 100; NO_2, 33; SO_2, 20.

(d) Limit concentration in CO_2: (ppmv): O_2, 1000; NO_2, 100; SO_2, 100.

Heterogeneities were considered through the use of seven "hydrological flow units" (HFUs), each defined with their own flow and mineralogical properties (Tables 3 and 4). It should be noted that the term "HFU", here, is somewhat of a misnomer because it is not used to define actual units in a stratigraphic sense, but to represent the grid-block by grid-block heterogeneous distribution of properties in the Petrel™ site geologic model. In this model, a specific mineralogy is assigned to each HFU, whereas porosity and permeability are heterogeneously distributed within each HFU, with average properties as listed in Table 3.

The less permeable and more clayey upper Precipice Sandstone was represented primarily by HFU #2 through #4, the “cleaner” and more permeable lower Precipice Sandstone primarily by HFU #5 through #7, and the Moolayember Formation primarily by HFU#1. Contrary to its lower member, the upper Precipice Sandstone has a significantly lower permeability and exhibits a notably different mineralogy that includes calcite, chlorite, and plagioclase.

Table 3. Model hydrologic properties (see Table 2 for a description of the simulated cases).

	HFU 1	**HFU 2**	**HFU 3**	**HFU 4**	**HFU 5**	**HFU 6**	**HFU 7**
Permeability (m^2)							
Cases A,A1,B	2.9×10^{-14}	4.2×10^{-14}	5.6×10^{-14}	3.4×10^{-13}	1.4×10^{-12}	1.7×10^{-12}	1.8×10^{-12}
Case B1	2.9×10^{-15}	1.4×10^{-14}	4.9×10^{-14}	1.6×10^{-13}	4.5×10^{-13}	1.3×10^{-12}	3.7×10^{-12}
Porosity							
Cases A,A1,B	0.054	0.067	0.084	0.12	0.17	0.19	0.19
Case B1	0.080	0.10	0.12	0.14	0.16	0.18	0.20
Capillary Pressure $1/P_0$ (Pa^{-1})							
Cases A, A1, B	8.4×10^{-4}	9.1×10^{-4}	9.3×10^{-4}	7.6×10^{-4}	6.0×10^{-4}	6.2×10^{-4}	3.5×10^{-4}
Case B1	2.4×10^{-4}	4.8×10^{-4}	8.2×10^{-4}	5.0×10^{-4}	3.4×10^{-4}	5.4×10^{-4}	4.5×10^{-4}
Relative Permeability							
S_{lr}	0.67	0.67	0.67	0.23	0.18	0.13	0.10
S_{gr} Cases A, A1, B	0.20	0.18	0.16	0.14	0.12	0.10	0.08
S_{gr} Case B1	0.27	0.27	0.27	0.47	0.44	0.40	0.30

Table 4. Concentrations of primary minerals specified in the simulations (wt %).

Minerals	HFU 1	HFU 2,3	HFU 4	HFU 5,6,7
Quartz	54.8	54.8	69.8	95.8
K-feldspar		5	12	1
Illite	20	10	12.5	
Kaolinite	10	20	5	3
Fe-Chlorite		7	0.5	
Calcite	5	3		
Siderite	0.2	0.1	0.2	0.1
Plagioclase (An10)	10			
Pyrite		0.1		
Goethite				0.1
In addition, the following potential secondary minerals were allowed to form: dolomite, ankerite, strontianite, chalcedony, magnesite, dawsonite, Ca-beideillite, albite (anhydrite also tested but never formed)				

To investigate the effect of increased concentrations of impurities, Case-A simulations were run with both the project "Target" (low) and "Limit" (high) concentrations of SO_2, NO_2, and O_2 in injected CO_2 (Table 2). Sensitivity analyses were also performed by running simulations with SO_2 and NO_2, but without O_2, and simulations with pure CO_2.

The porosity, permeability and mineralogy data were up- or down-scaled from the geologic grid as necessary to follow the discretization of the numerical model mesh. In the case of down-scaling for mesh refinement at the well (Fine Grid Case, Table 1), the information from coarser Petrel™ model grid blocks overlapping the finer numerical mesh was simply repeated in the smaller grid blocks. In contrast, in areas where the numerical mesh was set coarser to the geologic grid (away from the well), the porosity and permeability data from the geologic model were up-scaled by harmonic averaging, and the mineralogy was up-scaled by 1) counting the number of each HFU type (#1 to #7) within the area covered by each numerical model grid block, then 2) assigning the HFU type with the highest count.

Capillary properties and relative permeability as a function of saturation were simulated with the van Genuchten and Corey models for the liquid and CO_2 phases, respectively. Parameters for these models were fitted to drainage Leverett J-function data provided for each HFU by CTSco. Two ranges of CO_2 residual saturations were tested, a "Low" case with estimated values increasing with decreasing porosity, and a "High" case using values from imbibition data (Tables 2 and 3).

2.4. Initial conditions of temperature, pressure, and pore water composition

Initial steady conditions were set at hydrostatic pressure throughout the model domain. A temperature field was set following a linear regional geothermal gradient reflecting temperatures of 59.5°C at 840 m and 69°C at 1120 m BMSL, obtained from the drilling logs.

Computing steady (or quasi-steady) initial porewater compositions that reflect measured field data is another important pre-requisite of reactive-transport simulations. This was achieved by geochemical modeling to reconstruct the composition of deep waters accounting for the cooling and degassing that typically affect analyses at ground-surface temperature and pressure, with details provided in Spycher et al., (2018). Water analyses for this purpose were available only for the lower Precipice Sandstone (Table 5). A composition for the upper Precipice water was derived starting from these data and assuming reaction with formation minerals under a more reducing redox-state than in the lower sandstone, which was suggested by the lower permeability and presence of pyrite in the upper sandstone, compared to the more permeable lower member with ubiquitous goethite. The reconstructed water compositions (Table 5) were then used as input to 1000-year reactive-transport simulations under natural (no injection) conditions. The resulting near-steady field of porewater compositions and mineral abundances was then used as initial conditions for the simulations of CO_2 injection. The mineral amounts and water compositions resulting from these "ambient" simulations did not change appreciably from the data shown on Tables 4 and 5, except for precipitation of small quantities of ankerite (<0.5%) and negligible amounts of clay minerals, chalcedony, and albite (from albitization of plagioclase).

Table 5. Measured and reconstructed water compositions input into the model.

Species	**Units**	**Measured Concentration lower Precipice Sandstone**	**Reconstructed Concentration lower Precipice Sandstone**	**Reconstructed Concentration* upper Precipice Sandstone**
pH		6.8 at 65°C	6.66 at 65°C	6.92 at 65°C
Cl^-	mg/L	12.50	12.50	13
SO_4^{--}	mg/L	1.00	1.00	0.00
HCO_3^-	mg/L	100	140	1554
HS^-	mg/L as S	0.019	0.115	0.03
SiO_2	mg/L	29.9	30.0	30.0
Al^{+++}	mg/L	0.003	0.02	0.04
Ca^{++}	mg/L	0.35	0.35	10.0
Mg^{++}	mg/L	0.08	0.08	0.00
Fe^{++}	mg/L	1.10	1.36	0.194
K^+	mg/L	2.00	3.02	1.7
Na^+	mg/L	44.00	44.00	495
Sr^{++}	mg/L	0.007	0.007	0.01
F^-	mg/L	0.420	0.42	0.4
B	mg/L	0.034	0.034	0.03
Br^-	mg/L	0.080	0.080	0.08
Ba^{++}	mg/L	0.014	0.014	0.01

* Obtained starting from lower Precipice Sandstone water with $0.1xSO_4$, then reacted with quartz, K-feldspar, kaolinite, siderite, pyrite, calcite, chlorite, plagioclase (An10), and illite (proxy for muscovite).

2.5. CO_2 injection rate, simulated time period and time discretization

Model grid blocks representing the injection well were set to deliver the equivalent of a total CO_2 flow rate of 60 metric tons per year (3163 Mcsf/d, or 1.9 kg/s), for a total period of 3 years. The simulations covered an additional period of 97 years without injection (total simulated period of 100 years). The time discretization was dictated in large part by specifying a Courant Number of 0.5, which during the injection time period limited the time steps to about 12 hours with the Coarse grid, but significantly lower, to about 30 minutes, with the Fine grid.

2.6. Preliminary geochemical modeling

Reaction path models using Geochemist's Workbench (Bethke and Yeakel, 2012) were set up for the two major lithological units (lower and upper Precipice Sandstones), to further test the geochemical system investigated by the reactive-transport simulations. Good agreement was found for the principal trends in water composition evolution between reaction path and reactive-transport models. Details of this effort can be found in the full report for this project (Spycher et al., 2018).

3. RESULTS AND DISCUSSION

3.1. Effects of heterogeneity on the predicted CO_2 migration

In this study, the simulated CO_2 injection rate is rather small and the injection period short. In addition, the vertical permeability and porosity in the injection formation (lower Precipice Sandstone) are significantly higher than in the overlying upper unit. As a result, there is very little predicted migration of CO_2 laterally away from the injection zone, and essentially all the CO_2 is predicted to migrate quickly and vertically by buoyancy through the upper Precipice Sandstone until the geologic contact with the less permeable upper member, where it then spreads laterally (Figure 3). Because the CO_2 flow is buoyancy-dominated, the heterogeneities, resolution of the numerical grid and capillary properties of the formation have a significant impact on predicted flow patterns (e.g., Saadatpoor, 2009; Saadatpoor et al., 2009). It can be seen in Figure 3 that grid refinement (from Case A to A1) accompanied by increased gas residual saturation (from Case A1 to Case B), and increased capillary pressure heterogeneity (from Case B to Case B1) progressively result in more channelized flow and retention of CO_2 closer to the injection location. In all cases the predicted extent of the CO_2 plume at the time when injection stops (3 years) does not differ significantly from the predicted extent after 100 years, thus meaning that most of the CO_2 is trapped by capillary forces at the end of the injection period. The increase in CO_2 transport along vertical flow paths ('channelling') predicted with finer grids, particularly with Case B1, limits lateral migration but increases the penetration of CO_2 into the upper Precipice Sandstone.

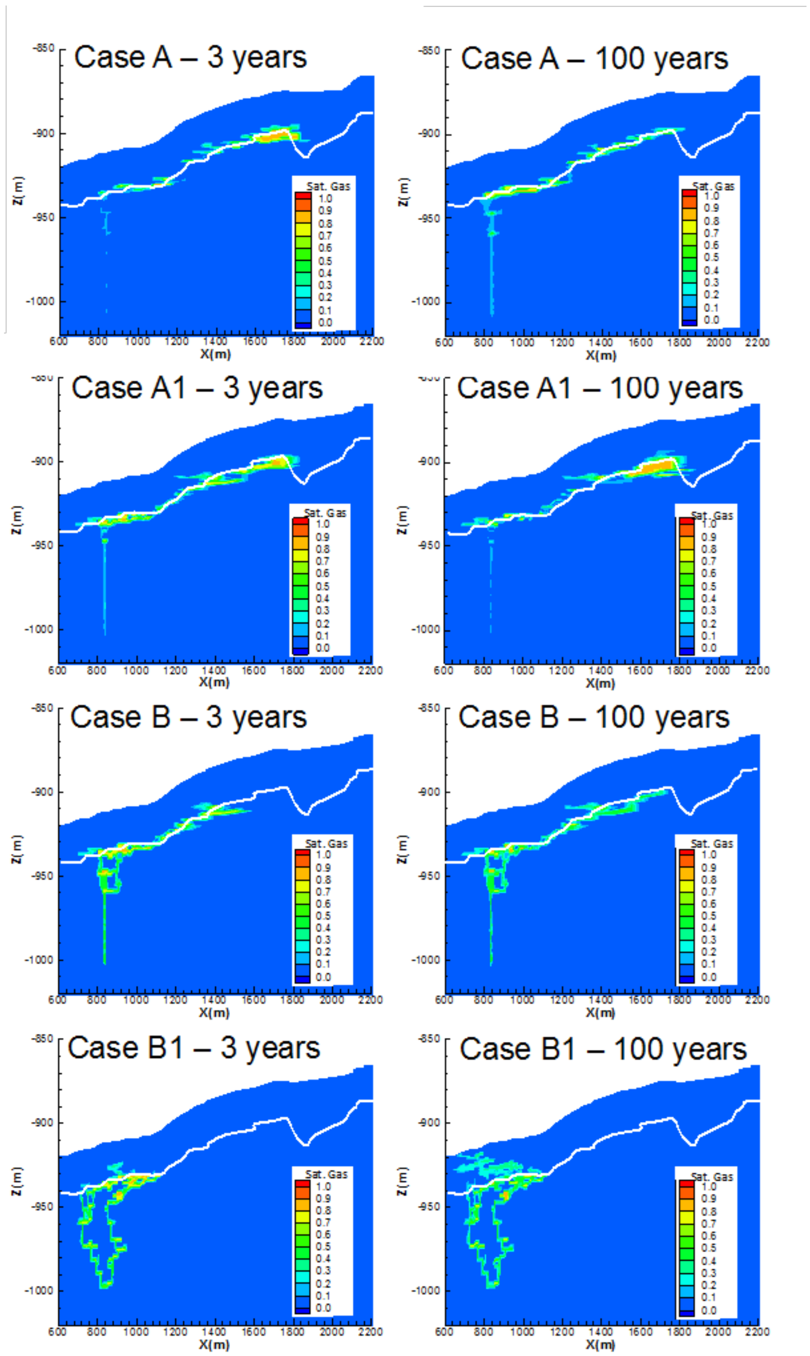

Figure 3. Predicted saturation of CO_2 after 3 years (end of injection period) and 100 years for cases with increasing: grid refinement (from Case A to A1); CO_2 residual saturation (from Case A1 to B); and capillary pressure heterogeneity (from Case B to B1). White line separates the lower from the upper Precipice Sandstone.

3.2. Dissolution, reactivity and accumulation of impurities

The predicted pH of the plume (Figure 4) follows closely the modeled CO_2 migration path, as the dissolution of CO_2 leads to the formation of carbonic acid in solution and lowers the formation water pH. Because calcite and other pH-buffering minerals are essentially absent from the lower Precipice Sandstone, the pH drops significantly from near-neutral background values down to ~ 4.6. On the contrary, the upper Precipice Sandstone contains pH-buffering minerals and a sharp pH gradient develops at the contact between these two members (Figure 4).

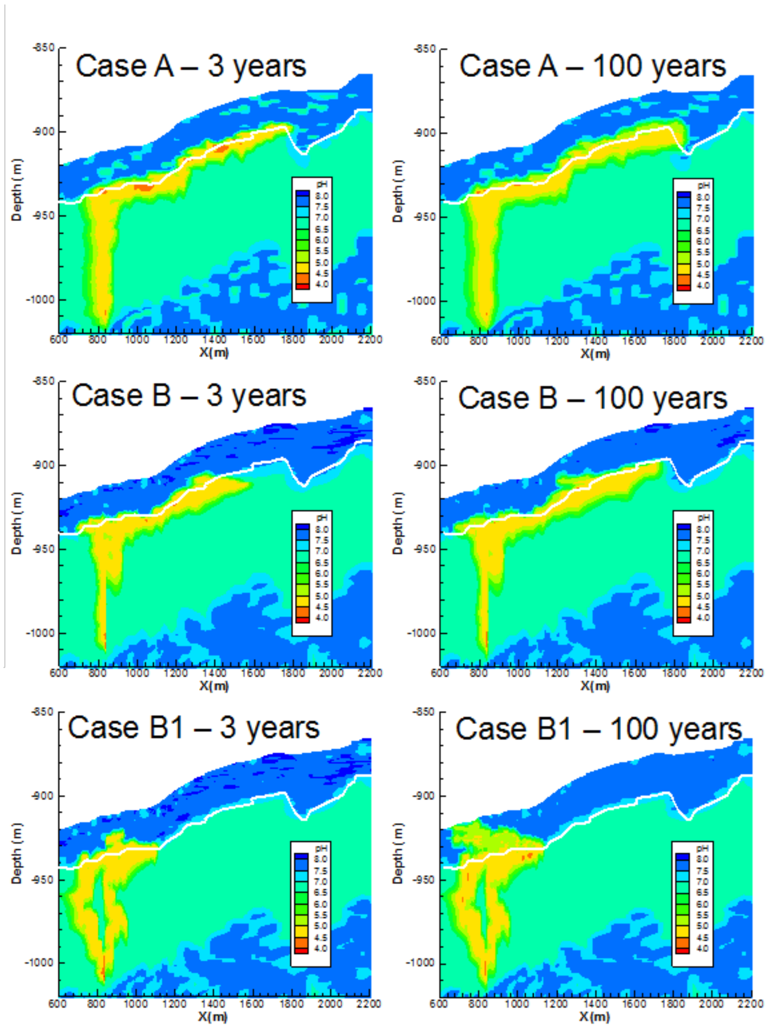

Figure 4. Predicted formation water pH after 3 and 100 years for Cases A, B, and B1, after injection of CO_2 with impurities at base-case concentrations. White line separates lower from upper Precipice Sandstone.

The pH of the plume seems unaffected by the co-injected impurities, except near the injection point where NO_2 and SO_2 dissolve and disproportionate almost immediately into the formation water (Eq. 1 - 3).

$$SO_{2(aq)} + H_2O \rightarrow 1.75\ H^+ + 0.25\ HS^- + 0.75\ SO_4^{-2} \qquad \log(K_{65°C}) = 0.94 \qquad (1)$$

$$R = k\,[SO_{2(aq)}] \qquad k = 2.7\times10^{-6} \qquad \text{(Möller, 1980)}$$

$$O_{2(aq)} + 0.5\ HS^- \rightarrow 0.5\ H^+ + 0.5\ SO_4^{-2} \qquad \log(K_{65°C}) = 60.03 \qquad (2)$$

$$R = k\,[O_{2(aq)}]^{0.82}\,[HS^-]^{0.2} \qquad k = 8.55\times10^{-5} \qquad \text{(Nielsen et al., 2003)}$$

$$2NO_{2(aq)} + H_2O \rightarrow 2\ H^+ + NO_2^- + NO_3^- \qquad \log(K_{65°C}) = -0.42 \qquad (3)$$

$$R = k\,[NO_{2(aq)}]^2 \qquad k = 8.4\times10^7 \qquad \text{(Park and Lee, 1988)}$$

The high solubility and fast reaction rates, irrespective of equilibrium or kinetic control, lead to a pH minimum and the accumulation of SO_4^{2-} and NO_3^- at the injection point (Figure 5). Such elevated "solubility" of NO_2 and SO_2, relative to that of CO_2, results in a chromatographic separation, whereby these impurities partition out of the CO_2 as soon as it contacts the formation water (Figure 5). This process further depresses the pH at the injection location, but only by a small amount when the low (target) impurity concentrations are considered: to pH ~ 4.4 in Case A, and to ~ 4.3 in Case B1, from values ~ 4.6 without impurities. At higher (limit) concentrations, the pH drops in the 2.5 to 3 range but only immediately adjacent to the well (Figure 4). It should be noted that when simulating the co-injection of NO_2 and SO_2 only (without O_2, at limit concentrations; Table 2), the pH is predicted to drop only to about 3.9 at the injection location. This indicates that the oxidation of sulfide (from SO_2 disproportionation) by co-injected O_2 (Eq. 2) is a significant driver of the increased pH drop (over that caused by CO_2) at the injection point when the higher concentrations of impurities are considered.

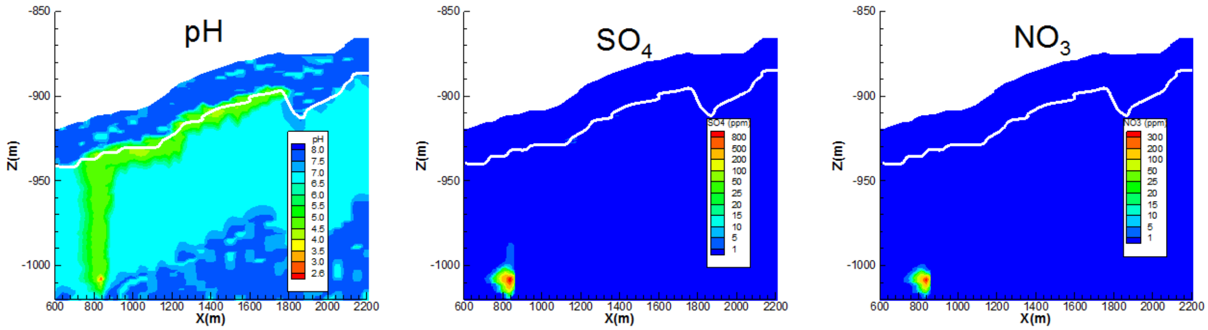

Figure 5. Distribution of pH, SO_4^{2-} and NO_3^- for Case A after three years of CO_2 injection with concentrations of 100 ppmv SO_2, 100 ppmv NO_2, and 1000 ppmv O_2 in the injected CO_2. Note the pH minimum and SO_4^{2-} and NO_3^- enrichments near the well because of reactions (1–3). White line separates lower from upper Precipice Sandstone.

Because the disproportionation of SO_2 and NO_2 is essentially immediate (and never reaches solubility limits), the predicted dissolved concentrations of these gases (i.e., $SO_{2(aq)}$ and $NO_{2(aq)}$) are essentially nil, except directly at the injection point when reactions (Eq. 1–3) are implemented with kinetic constraints (Figure 6). In this case, the maximum concentrations of $NO_{2(aq)}$ at the injection point (at the end of the injection period) reaches about 0.1 ppm at the well and drops down essentially to zero within a few tens of centimeters from the injection point (not shown). A similar behaviour is predicted for $SO_{2(aq)}$, except that in this case the predicted dissolved concentration directly at the injection point is more significant (up to about 50 ppm), and minor vertical migration of SO_2 is predicted to occur but only until the end of the injection period (3 years, Figure 6). The precipitation of calcium sulfate minerals (anhydrite, gypsum) from the oxidation of co-injected SO_2 is not predicted because reactive ca-bearing minerals (calcite, plagioclase) are essentially absent in the formation around the injection zone.

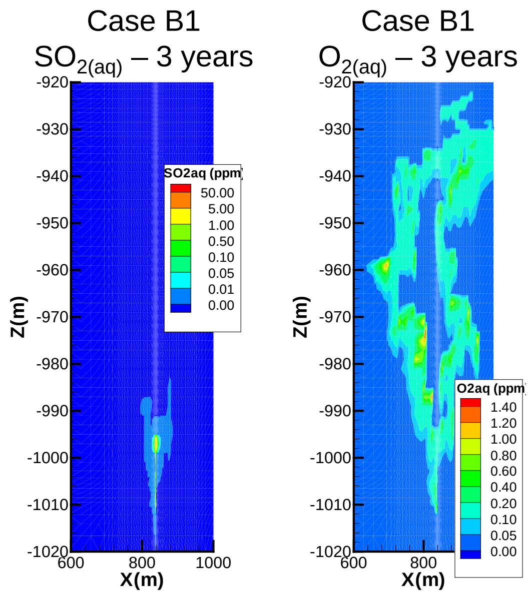

Figure 6. Predicted concentrations of dissolved $SO_{2(aq)}$ and $O_{2(aq)}$ after 3 years of CO_2 injection in the vicinity of the injection well (the injection interval is at Z = -1010 to -1007 m BMSL, and centered at X = 837.5 m), considering the Fine numerical mesh and kinetic dissolution. At later time $SO_{2(aq)}$ disappears, and the concentration of $O_{2(aq)}$ slowly drops. With a coarser grid and under equilibrium constraints, the concentrations of these dissolved gases are essentially nil. In all cases considered the concentration of $NO_{2(aq)}$ is essentially nil because the reaction (Eq. 3) is extremely fast.

At thermodynamic equilibrium, co-injected O_2 is immediately consumed by the oxidation of sulfide (Eq. 2) produced by the disproportion of SO_2 (Eq. 1). In this case no oxygen is predicted to migrate away from the injection point, and dissolved oxygen concentrations are essentially nil. However, when slowing this oxidation using typical rates from the literature, co-injected O_2 is not entirely consumed by sulfide/SO_2 oxidation. Some of it is transported along with the CO_2 and is predicted to dissolve mostly at sub-ppm levels away from the injection point (Figure 6). Because O_2 is less soluble than CO_2, this gas tends to become enriched in the supercritical CO_2 phase, particularly at locations where CO_2 remains trapped by capillary forces, causing the spotty appearance of the $O_{2(aq)}$ contour plot in Figure 6. Therefore, whereas NO_2 and SO_2 disproportionation products concentrate near the source, O_2 may migrate further away if its reduction is impeded by kinetic constraints.

These simulations also show that the predicted effect of NO_2 and SO_2 disproportionation near the injection point does not only depend on the concentration of these impurities in the injected CO_2, but is also sensitive to the spatial resolution of the numerical grid. This is because the dissolution of small, finite amounts of these compounds into large model grid blocks can never reach solubility limits. Thus, large grid blocks at the injection point effectively cause a dilution of the dissolved concentrations of NO_2 and SO_2 at this location, resulting in higher pH values than in finely discretized grids.

3.3. CO_2 mineralization

The dissolution of CO_2 drives a series of mineral reactions giving rise to solute concentrations that initially increase along the path of the CO_2 plume and then, for many constituents, decrease when secondary minerals start to precipitate. In general, the injection of CO_2 (with or without impurities) cause an increase in dissolved K, Ca, Mg, Fe and silica in the upper Precipice Sandstone, whereas only (and less pronounced) dissolved K, Fe and silica rise in the lower Precipice Sandstone. The difference is due to the difference in the mineral composition of these two sandstones, with more reactive minerals (K-feldspar, calcite and Fe-chlorite) in the upper member, compared to the much "cleaner" lower member (Table 4). In all simulated cases, the most significant mineral dissolution and precipitation take place at and above the contact between the lower and upper Precipice Sandstones. The main reactions with CO_2 consist of the dissolution of primarily Fe-chlorite and calcite and the precipitation of ankerite, kaolinite, magnesite, and silica (here modelled as chalcedony):

$$\underset{\text{(Fe-chlorite)}}{Fe_{3.5}Mg_{1.5}\,Al_2Si_3O_{10}(OH)_8} + 5\,CO_2 + \underset{\text{(calcite)}}{3.5\,CaCO_3} \rightarrow$$

$$3.5\ CaFe(CO_3)_2 + Al_2Si_2O_5(OH)_4 + SiO_2 + 1.5\ MgCO_3 + 2\ H_2O$$
(ankerite) (kaolinite) (chalcedony) (magnesite)

Illitisation of K-feldspar is also predicted to be pervasive in both the upper and lower Precipice Sandstone, although with much less intensity than the alteration of chlorite and calcite. Only the mobilization of Fe and Mg from the dissolution of chlorite may lead to a net carbon mineralization in form of ankerite and magnesite, but those reactions only contribute to a very minor degree to carbon trapping. These results are in line with results of previous modeling and experimental studies (e.g., Xu et al., 2007, 2010; Luquot et al., 2012; Kharaka et al., 2006, 2010; Wilke et al., 2012; Erickson et al., 2015; Pearce et al., 2015; Wei et al., 2015; de Dios et al., 2016; Waldmann and Rütters, 2016; Vu et al., 2017, 2018).

The computed overall porosity change from these reactions is small and negative (about -0.3% at 100 years; Figure 7). As a result, the predicted effect on flow is insignificant, and flow simulations that do not consider the effects of geochemical reactions yield essentially identical CO_2 plume migration patterns.

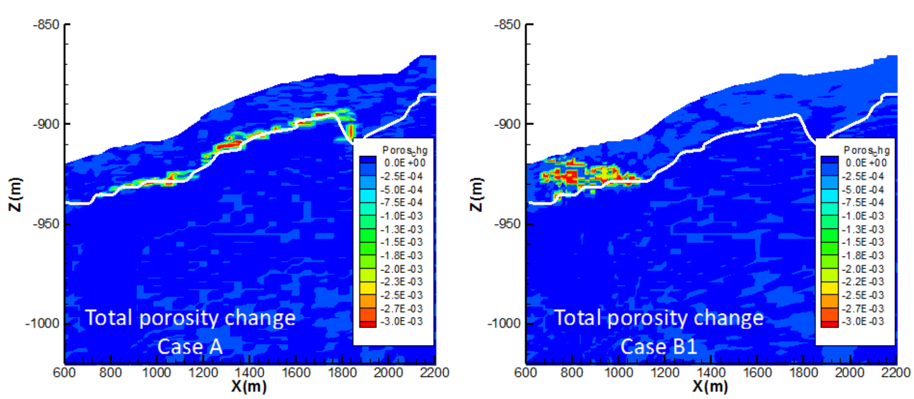

Figure 7. Predicted total (overall) porosity change after 3 years of injection and 97 years post-injection in Case A and Case B1 (volume fraction units). The injection interval is at Z = -1010 to -1007 m BMSL, centered at X = 837.5 m.

4. CONCLUSIONS

CO_2 migration in the lower Precipice Sandstone is primarily buoyancy-controlled because of the high porosity and permeability of this formation, and the somewhat low CO_2 injection rate considered. Heterogeneities in flow properties (porosity, permeability, and capillarity), when modeled with a numerical mesh refined to < 0.5 m near the injection well, together with increased residual gas saturation and capillary entry pressure, result in increased channelized flow compared to less refined models. In the present case, the more refined models yield restrained lateral CO_2 migration, but more vertical penetration of CO_2 into the upper Precipice Sandstone. In contrast, a greater extend of lateral CO_2 migration and more significant accumulation of CO_2 closer to the contact between the upper and lower Precipice Sandstones is predicted in case of more homogenous CO_2 flow. This points out to the importance of evaluating the effects of both 1) heterogeneities and 2) mesh refinement when applying numerical models to investigate CO_2 injection into the subsurface. In a first of its kind this study includes the effect of fine scale heterogeneity in reactive-transport simulations towards the assessment of CO_2 geological sequestration.

The co-injected CO_2 impurities SO_2 and NO_2 (at concentrations $\leqslant$ 100 ppmv) are highly soluble under reservoir conditions and modeled to be rapidly stripped out of the CO_2 stream, resulting in the chromatographic separation of these impurities near their injection point. The oxidation of these impurities leads to acid formation in addition to the effect of CO_2 dissolution. This effect is exacerbated if O_2 is also co-injected (here at concentrations $\leqslant$ 1000 ppmv in CO_2), as oxygen further contributes to the oxidation of SO_2 and associated acid formation. Acid levels exceeding acid formation from CO_2 dissolution only are expected to be noticeable in the immediate vicinity of the injection point. At this location, modeled pH values depend not only on the impurities concentrations and the time of injection, but are quite sensitive to the degree of model mesh refinement near the well.

The essentially negligible impact of impurities away from the injection well is in contrast to some studies showing more effect, primarily because of significantly higher concentrations of impurities in CO_2 (Renard et al., 2014; Wilke et al., 2012; Corvisier et al., 2013; Jung et al., 2013; Erickson et al., 2015; Pearce et al., 2015). However, there is a lack of consistent published experimental data to model with confidence the partitioning and dissolution kinetics of NO_2, SO_2, and O_2 from CO_2 streams into groundwater. For example, a recent experimental study by Amshoff et al. (2018) suggests that the transfer of SO_2 from CO_2 may be over-predicted when using the thermodynamic models implemented in the present study. In contrast, a recent field experiment (Vu et al., 2017, 2018) seems to confirm the results of the present study, also concluding that the impact of O_2 and SO_2 impurities (at concentration of 6150 ppm and 67 ppm, respectively) is minimal. It is therefore likely that accurate predictive modeling of SO_2, O_2, and NO_2, particularly regarding pH near wells under injection conditions, is likely to require more experimentally verified and consistent kinetic dissolution models than currently available. Smaller-scale, more refined numerical meshes than those implemented here would also raise the confidence in predictive model results close to injection zones.

As shown in previous modeling studies of CO_2 geologic sequestration, the solute plume is primarily controlled by the migration of free phase (supercritical) CO_2 and is characterized by low pH (ranging ~ 4 and above) and increased dissolved ion concentrations. The dissolution of CO_2 drives a series of reactions primarily at and above the contact between the upper and lower Precipice Sandstones, however resulting in a negligible overall porosity change over a period of 100 years. At this location, the simulations show that even minor concentrations (< 5 wt%) of reactive minerals such as Fe-chlorite, calcite, and K-feldspar lead to a significant enrichment in cations such as calcium, iron, potassium and magnesium in the solute plume within the first three years after commencement of the injection. Therefore, this zone could be a good candidate for water quality monitoring.

ACKNOWLEDGMENTS

The authors wish to acknowledge financial assistance provided through Australian National Low Emissions Coal Research and Development (ANLEC R&D). ANLEC R&D is supported by COAL21 Ltd and the Australian Government through the Clean Energy Initiative. We also thank the Carbon Transport and Storage Company (CTSCo) for providing data and engaging in discussions for this project.

REFERENCES

Alekseyev, V.A., 2007. Equations for the dissolution reaction rates of montmorillonite, illite, and chlorite. Geochemistry International 45 (8), 770-780.

Amshoff, P., Weger, T., Ostertag-Henning, C., 2018. Dissolution kinetics of CO_2 and CO_2-SO_2 mixtures in water and brine at geological storage conditions of 16 MPa and 333 K. International Journal of Greenhouse Gas Control 79, 173-180.

Arnórsson, S., Stefánsson, A., 1999. Assessment of feldspar solubility constants in water in the range of 0° to 350 °C at vapor saturation pressures. American Journal of Science. 299, 173-209.

Barin, I., Platzki, G., 1995. Thermochemical data of pure substances. (3rd Edition). Weinheim, Germany; New York, NY: VCH. TIC: 251934.

Bénézeth, P., Palmer, D.A., Anovitz, L.M., Horita, J., 2007. Dawsonite synthesis and reevaluation of its thermodynamic properties from solubility measurements: Implications for mineral trapping of CO_2. Geochimica et Cosmochimica Acta 71 (18), 4438-4455.

Bethke, C.M., Yeakel, S., 2012. The Geochemist's Workbench Release 9.0, Aqueous Solutions LLC.

Brandt, F., Bosbach, D., Krawczyk-Bärsch, E., Arnold, T., Bernhard, G., 2003. Chlorite dissolution in the acid pH-range: a combined microscopic and macroscopic approach. Geochimica et Cosmochimica Acta 67(8), 1451-1461.

Corvisier, J., Bonvalot, A.-F., Lagneau, V., Chiquet, P., Renard, S., Sterpenich J., Pironon, J., 2013. Impact of co-injected gases on CO_2 storage sites: Geochemical modeling of experimental results. Energy Procedia 37, 3699-3710.

de Dios, J.C., Delgado, M. A., Marín, J. A., Martinez, C., Ramos, A., Salvador, I., Valle, L., 2016. Short-term effects of impurities in the CO_2 stream injected into fractured carbonates. International Journal of Greenhouse Gas Control 54, Part 2, 727-736.

Duckworth, O.W., Martin, S. T., 2004. Role of molecular oxygen in the dissolution of siderite and rhodochrosite. Geochimica et Cosmochimica Acta 68 (3), 607-621.

Erickson, K. P., Lempp, C., Pöllmann, H., 2015. Geochemical and geomechanical effects of $scCO_2$ and associated impurities on physical and petrophysical properties of Permotriassic Sandstones (Germany): an experimental approach. Environmental Earth Sciences 74(6), 4719-4743.

Garcia, S., Rosenbauer, R.J., Palandri, J., Maroto-Valer, M.M., 2012. Sequestration of non-pure carbon dioxide streams in iron oxyhydroxide-containing saline repositories. International Journal of Greenhouse Gas Control 7, 89-97.

Golubev, S., Bénézeth, P., Schott, J., Dandurand, J., Castillo, A., 2009. Siderite dissolution kinetics in acidic aqueous solutions from 25 to 100 °C and 0 to 50 atm pCO_2. Chemical Geology 265, 13-19.

Gunter, W.D., Perkins, E.H., Hutcheon, I., 2000. Aquifer disposal of acid gases: modelling of water–rock reactions for trapping of acid wastes, Applied Geochemistry Volume 15, Issue 8, 1085-1095.

Hedayati, M., Wigston, A., Wolf, J.L., Rebscher, D., Niemi, A., 2018. Impacts of SO_2 gas impurity within a CO_2 stream on reservoir rock of a CCS pilot site: Experimental and modelling approach. International Journal of Greenhouse Gas Control 70, 32-44.

Helgeson, H.C., Delany, J. M., Nesbitt, H.W., Bird, D. K., 1978. Summary and critique of the thermodynamic properties of rock-forming minerals, American Journal of Science 278, 1-229.

Hellevang H., Declercq, J., Kvamme, B., Aagaard, P., 2010. The dissolution rates of dawsonite at pH 0.9 to 5 and temperatures of 22, 60 and 77 ^oC. Applied Geochemistry Vol 25, Issue 10, 1575-1586.

Holland, T.J.B., Powell, R., 1998. An internally consistent thermodynamic data set for phases of petrological interest. Journal of Metamorphic Geology 16(3), 309-343.

Islam, M.R., Chakma, A., 1993. Storage and utilization of CO_2 in petroleum reservoirs: a simulation study. Energy Conversion and Management 34 (9-11), 1205-1212.

Jung, H. B., Um, W., Cantrell, K.J., 2013. Effect of oxygen co-injected with carbon dioxide on Gothic shale caprock–CO_2–brine interaction during geologic carbon sequestration. Chemical Geology, 354: 1-14.

Kharaka, Y.K., Cole, D.R., Hovorka, S.D., Gunter, W.D., Knauss K.G., Freifeld, B.M., 2006. Gas-water-rock interactions in Frio Formation following CO_2 injection: Implications for the storage of greenhouse gases in sedimentary basins. Geology 34(7), 577-580.

Kharaka, Y.K., Thordsen, J.J., Kakouros, E., Ambats, G., Herkelrath, W.N., Beers, S.R., Birkholzer, J.T., Apps, J.A., Spycher, N.F., Zheng, L., Trautz, R.C., Rauch H.W., Gullickson, K.S., 2010. Changes in the chemistry of shallow groundwater related to the 2008 injection of CO_2 at the ZERT field site, Bozeman, Montana. Environmental Earth Sciences 60(2), 273-284.

Knauss, K.G., Johnson, J.W., Steefel, C.I., 2005. Evaluation of the impact of CO_2, co-contaminant gas, aqueous fluid, and reservoir rock interactions on the geologic sequestration of CO_2. Chemical Geology 217, 339-350.

Luquot, L., Andreani, M., Gouze, P., Camps, P., 2012. CO_2 percolation experiment through chlorite/zeolite-rich sandstone (Pretty Hill Formation – Otway Basin–Australia). Chemical Geology 294-295, 75-88.

Miri, R., Aagaard, P., Hellevang, H., 2014. Examination of CO_2–SO_2 Solubility in Water by SAFT1. Implications for CO_2 Transport and Storage. The Journal of Physical Chemistry B 118 (34), 10214-10223.

Möller, D., 1980. Kinetic model of atmospheric SO_2 oxidation based on published data. Atmospheric Environment Vol. 14, 1067-1076.

Nielsen, A.H., Vollersten, J., Hvitved-Jacobsen, T., 2003. Determination of kinetics and stoichiometry of chemical sulfide oxidation in wastewater of sewer networks. Environmental Science and Technology. 37, 3853-3858.

Palandri, J.L., Kharaka, Y.K., 2004. A compilation of rate parameters of water-mineral interaction kinetics for application to geochemical modeling, National Energy Technology Laboratory – United States Department of Energy.

Palandri, J.L., Kharaka, Y.K., 2005. Ferric iron-bearing sediments as a mineral trap for CO_2 sequestration: Iron reduction using sulfur-bearing waste gas. Chemical Geology 217, 351-364.

Park J-Y., Lee Y-N., 1988. Solubility and decomposition kinetics of nitrous acid in aqueous solution. The Journal of Physical Chemistry 92, 6294-6302

Pearce, J.K., Kirste, D.M., Dawson, G.K.W., Farquhar, S.M., Biddle, D., Golding, S.D., Rudolph, V., 2015. SO_2 impurity impacts on experimental and simulated CO_2–water–reservoir rock reactions at carbon storage conditions. Chemical Geology 399, 65-86.

Perkins, E.H., Gunter, W.D., 1995. Aquifer disposal of CO_2-rich greenhouse gases: Modelling of water-rock reaction paths in a siliciclastic aquifer. In: Kharaka, Y.K., Chudaev, O.V. (Eds.), Proc. 8th International Symposium On Water-Rock Interaction. Balkema, Rotterdam, 895-898.

Pruess, K., Spycher, N., 2007. ECO2N – A Fluid property module for the TOUGH2 code for studies of CO_2 storage in saline aquifers. Energy Conversion and Management 48 (6), 1761-1767.

Renard, S., Sterpenich, J., Pironon, J., Chiquet, P., Randi, A., 2014. Geochemical effects of an oxycombustion stream containing SO_2 and O_2 on carbonate rocks in the context of CO_2 storage. Chemical Geology 382, 140-152.

Sin, I., Lagneau, V., Corvisier, J. (2017) Integrating a compressible multicomponent two-phase flow into an existing reactive transport simulator. Advances in Water Resources 100, 62–77.

Saadatpoor, E., Bryant, S.L., Sepehrnoori, K., 2009. Upscaling local CO_2 trapping during bouyancy driven flow. SPE 124846.

Saadatpoor, E., 2009. Effect of capillary heterogeneity on buoyant plumes: new trapping mechanism in carbon sequestration. M.S. thesis, The University of Texas at Austin, Austin, Texas.

Shock, E.L., Sassani, D.C., Willis, M., Sverjensky, D. A., 1997. Inorganic species in geologic fluids: Correlations among standard molal thermodynamic properties of aqueous ions and hydroxide complexes. Geochimica et Cosmochimica Acta 61, 907-950.

Slider, H.C., 1976. Practical petroleum reservoir engineering methods, An Energy Conservation Science. Tulsa, Oklahoma, Petroleum Publishing Company.

SNL (Sandia National Laboratories), 2007. Qualification of thermodynamic data for geochemical modeling of mineral–water interactions in dilute systems (eds. Wolery, T. J., Jove Colon, C. F.), Report ANL-WIS-GS-000003 REV 01. Las Vegas, Nevada: Sandia National Laboratories. ACC: DOC.20070619.0007.

Sonnenthal, E., Spycher, N., Xu, T., Zheng, L., Miller, N., Pruess, K., 2014. TOUGHREACT V3.0-OMP reference manual: A parallel simulation program for non-isothermal multiphase geochemical reactive transport . Lawrence Berkeley National Laboratory , Berkeley, CA.

Spycher, N., Oldenburg, C., 2014. Will mercury impurities impact CO_2 injectivity in deep sedimentary formations? II. Mineral dissolution and precipitation. Greenhouse Gases: Science and Technology 5(1), 72-90.

Spycher, N., Llanos, E.M., Vu, H.P., Haese, R.R., 2018. Modelling of a solute plume composition in the Surat Basin (Queensland). ANLEC Confidential Report. Reference No. 71116-0290.

Talman, S. (2015) Subsurface geochemical fate and effects of impurities contained in a CO_2 stream injected into a deep saline aquifer: What is known. International Journal of Greenhouse Gas Control, (40), 267-291.

Tan, S.P., Piri, M., 2013. Modeling the solubility of nitrogen dioxide in water using perturbed-chain statistical associating fluid theory. Industrial & Engineering Chemistry Research 52 (45), 16032-16043.

Thaysen, E.M., Soler, J.M., Boone, M., Cnudde, V., Cama, J., 2017. Effect of dissolved H_2SO_4 on the interaction between CO_2-rich brine solutions and limestone, sandstone and marl. Chemical Geology 450, 31-43.

Todaka, N., Xu, T., 2017. Reactive transport simulation to assess geochemical impact of impurities on CO_2 injection into siliciclastic reservoir at the Otway site, Australia. International Journal of Greenhouse Gas Control 66, 177-189.

Vu, H.P., Black, J.R., Haese, R.R., 2017. Changes in formation water composition during water storage at surface and post re-injection. Energy Procedia 114 (Supplement C), 5732-5741.

Vu, H.P., Black, J.R., Haese, R.R., 2018. The geochemical effects of O_2 and SO_2 as CO_2 impurities on fluid-rock reactions in a CO_2 storage reservoir, International Journal of Greenhouse Gas Control 68, 86-98.

Wagman, D.D., Evans, W.H., Parker, V.B., Schumm, R.H., Halow, I., Bailey, S.M., Churney, K.L., and Nuttall, R.L., 1982. The NBS tables of chemical thermodynamic properties: Selected values for inorganic and C_1 and C_2 organic substances in SI Units. Journal of Physical and Chemical Reference. Data, 11, supp. 2, 392 p.

Waldmann, S., Rütters, H., 2016. Geochemical effects of SO_2 during CO_2 storage in deep saline reservoir sandstones of Permian age (Rotliegend) – A modeling approach. International Journal of Greenhouse Gas Control 46, 116-135.

Wei, N., Li, X., Wang, Y., Zhu, Q., Liu, S., Liu, N., Su, X., 2015. Geochemical impact of aquifer storage for impure CO_2 containing O_2 and N_2: Tongliao field experiment. Applied Energy 145, 198-210.

Wilke, F.D.H., Vásquez, M., Wiersberg, T., Naumann, R., Erzinger, J., 2012. On the interaction of pure and impure supercritical CO_2 with rock forming minerals in saline aquifers: An experimental geochemical approach. Applied Geochemistry 2**7**(8), 1615-1622.

Wolf, J.L., Niemi, A., Bensabat, J., Rebscher, D., 2016. Benefits and restrictions of 2D reactive-transport simulations of CO_2 and SO_2 co-injection into a saline aquifer using TOUGHREACT V3.0-OMP, International Journal of Greenhouse Gas Control 54 (2), 610-626.

Xu, T., Spycher, N., Sonnenthal, E., Zhang, G., Zheng, L., Pruess, K., 2011. TOUGHREACT Version 2.0: A simulator for subsurface reactive transport under non-isothermal multiphase flow conditions. Computers & Geosciences 37, 763-774.

Xu, T., Apps, J.A., Pruess, K., Yamamoto, H., 2007. Numerical modeling of injection and mineral trapping of CO_2 with H_2S and SO_2 in a sandstone formation. Chemical Geology 242, 319-346.

Xu, T., Kharaka, Y.K., Doughty, C., Freifeld, B.M,. Daley, T.M., 2010. Reactive-transport modeling to study changes in water chemistry induced by CO_2 injection at the Frio-I Brine Pilot. Chemical Geology 271(3–4), 153-164.

Yang, L., Steefel, C.I., 2008. Kaolinite dissolution and precipitation kinetics at 22°C and pH 4. Geochimica et Cosmochimica Acta 72(1), 99-116.

Ziabakhsh-Ganji, Z., Kooi, H., 2012. An equation of state for thermodynamic equilibrium of gas mixtures and brines to allow simulation of the effects of impurities in subsurface CO_2 storage. International Journal of Greenhouse Gas Control 11S, S21-S24.

Appendix A. Input Thermodynamic and Kinetic Data

Thermodynamic data were taken from a database (SNL, 2007) derived in large part from Shock et al. (1997) and Helgeson et al. (1978). The solubilities of SO_2, NO_2 and O_2 in this database were originally derived from reference data in Shock et al. (1997) for aqueous species, and Barin and Platzki (1995) and Wagman et al. (1982) for gaseous species. This database was updated with solubility data for kaolinite from Yang and Steefel (2008), plagioclase and feldspars from Arnórsson and Stefánsson (1999) (corrected for consistency with the quartz solubility in the database), dawsonite from Bénézeth et al. (2007), and Fe-chlorite computed assuming an ideal solid solution of 30 mol% chlorite (Mg end-member) and 70 mol% daphnite (Fe end-member) using data from Holland and Powell (1998).

Kinetic rate laws and constants, and activation energies, were taken from the literature, primarily from the compilation of Palandri and Kharaka (2004). These data and their sources are listed in Table A.1. Mineral specific surface areas shown on these table were estimated as the geometric surface area of packed spheres with grain size based on site-specific data (varying from 60 to 2000 µm), and assuming clay minerals to have 10x larger surface areas than other minerals.

Table 3.3-1. Minerals and their kinetic data used in simulations

Minerals	Specific Surface Area (m^2/m^3)	Temkin coefficient	Parameters for kinetic rate law								Source[7]
			Neutral mechanism		Acid/other mechanism			Base/other mechanism			
			Log(k_{25})	E_a	Log(k_{25})	E_a	n (H^+)	Log(k_{25})	E_a	n (H^+)	
Quartz	10^3	1.0	-13.34	90.1	-	-	-	-	-	-	a
K-feldspar	10^4	0.333	-12.41	38.0	-10.06	51.7	0.5	-21.2	94.1	-0.823	a
Illite[1]	10^5	0.333	-13.55	22.0	-11.85	22.0	0.37	-14.55	22.0	-0.22	a
Kaolinite	10^4	0.333	-12.97	22.2	-11.10	65.9	0.777	-16.84	17.9	-0.472	b
Fe-Chlorite	10^4	0.333	-13.00	60.0	-9.79	60.0	0.49	-10.77	60.0	0.43	c
Calcite	10^4	1.0	-5.81	23.5	-0.3	14.4	1.0	-3.48	35.4	1.0 (CO_3^{-2})	a
Siderite	10^4	1.0	-8.65	48.0	-3.75	48.0	0.75	-	-	-	d
Plagioclase (An10)[2]	10^4	1.0	-11.83	69.8	-9.67	65	0.457	-	-	-	a
Pyrite	10^4	1.0	-	-	-9.1	56.9	-0.11 (H^+) 0.5 (O_{2aq})	-9.58	56.9	-0.32 (H^+) 0.3 (Fe^{+3}) -0.47 (Fe^{+2})	a
Goethite	10^4	1.0	-7.94	86.5	-	-	-	-	-	-	a
Dolomite	10^4	1.0	-7.53	52.2	-3.18	36.1	0.5	-5.11	34.8	0.5 (CO_3^{-2})	a
Ankerite[3]	10^4	1.0	-8.65	48	-3.75	48.0	0.75	-	-	-	a
Strontianite[4]	10^4	1.0	-5.81	23.5	-0.3	14.4	1.0	-3.48	35.4	1.0 (CO_3^{-2})	a
Chalcedony (dissol.)	10^4	1.0	-12.14	60.9	-	-	-	-	-	-	a
Chalcedony (precip.)	10^4	4.4	-10.0	0.	-	-	-	-	-	-	a
Magnesite	10^4	1.0	-9.34	23.5	-6.38	14.4	1.0	-5.22	62.8	1.0	a
Dawsonite[5]	10^4	1.0	-8.66	63.82	-4.48	49.43	0.982	-	-	-	e
Ca-Beideillite[6]	10^5	0.286	-12.78	35	-10.98	23.6	0.34	-16.52	58.9	-0.4	a
Albite	10^4	0.333	-12.56	69.8	-10.16	65	0.457	-15.6	71	-0.572	a

[1] Data for muscovite. [2] Data for oligoclase. [3] Data for siderite. [4] Data for calcite. [5] For precipitation, assumed neutral rate cut 10-fold from value shown, and acid mechanism not implemented. [6] Data for smectite. [7] Data sources: [a] Palandri and Kharaka 2004; [b] Yang and Steefel 2008; [c] Alekseyev 2007 and Brandt et al. 2003; [d] Golubev et al. 2009, and Duckworth and Martin 2004; [e] Hellevang et al., 2010.

.